

CNN on ‘Top’

In Search of Scalable & Lightweight Image-based Jet Taggers

Rajneil Baruah^{a,1}, Subhadeep Mondal^{b,1}, Sunando Kumar Patra^{c,2}, Satyajit Roy^{d,2}

¹Department of Physics, SEAS, Bennett University, Greater Noida, Uttar Pradesh, 201310, India

²Department of Physics, Bangabasi Evening College, Kolkata, 700009, West Bengal, India

Received: date / Accepted: date

Abstract While Transformer-based and standard Graph Neural Networks (GNNs) have proven to be the best performers in classifying different types of jets, they require substantial computational power. We explore the scope of using a lightweight and scalable version of *EfficientNet* architecture, along with global features of the jet. The end product is computationally inexpensive but is capable of competitive performance. We showcase the efficacy of our network in tagging top-quark jets in a sea of other light quark and gluon jets. The work also sheds light on the importance of global features for both the accuracy and the apparent redundancy of the network’s complexity.

1 Introduction

As we enter the high-energy (HE) and high luminosity (HL) phase of the Large Hadron Collider (LHC), the study of jet physics has become more relevant than ever. ‘Fat jet tagging’ is a critical task for identifying the hadronic decays of massive particles, such as the Higgs boson, top quark, or a W or Z -boson that are produced with high momentum or ‘boost’ in a particular direction. As a result of this boost, the decay products of these standard model (SM) particles are highly collimated and can be contained within a single large-radius jet, which we call a ‘fat jet’. Scenarios like this can easily occur in various beyond the standard model (BSM) frameworks with vector-like quarks [1, 2], leptoquarks [3–5], heavy right-handed neutrinos [6, 7], supersymmetric particles with R -parity violating couplings [8, 9], to name a few. Among the above-mentioned SM particles, top quark

holds a unique status. It happens to be the heaviest fundamental particle we know thus far, and unlike other quarks, it decays before hadronization. The heavy mass of the top quark means its coupling strength with the Higgs boson is the strongest. Hence, precise measurements of top quark properties provide a consistency check of the SM. Even subtle deviations from the SM predictions for top quark interactions could hint at new physics. Moreover, the top quark mass plays a crucial role in determining the stability of the electroweak vacuum. Though the current measurements suggest that our vacuum is ‘metastable’ [10–12], this conclusion is highly sensitive to the precise values of the top quark measurements [13–15]. Identifying top quark jets as fat jets in a sea of other light quark and gluon jets, therefore, is a rather important task.

Machine learning (ML) has revolutionized this field [16–18] by moving beyond traditional methods that relied on high-level, physics-inspired features like jet mass, jet radius, n -subjettiness, energy correlation functions, etc [19–31]. Deep learning models, on the other hand, instead of using simple, hand-crafted features, train themselves to represent the jets as points in a vector space of features best suited for the subsequent classification. The inputs to these models include the four-momentum components of each constituent particle, global features that carry the kinematical properties of the jet, and particle tracking IDs whenever available. From the ML perspective, the jet physics task at hand can be divided into two broad categories: classification and generation. Both of these ‘downstream’ tasks depend on representing the raw, low-level particle or detector data associated with a jet as points in a dense, continuous vector space (feature space), ready to be effectively processed by any ML algorithm. This process, known as ‘embedding/encoding,’ allows the model to learn a more comprehensive and nuanced representation of the substructure of a jet, which can be utilized in subsequent downstream tasks.

^ae-mail: rajneilb.physics@gmail.com

^be-mail: subhadeep.mondal@bennett.edu.in

^ce-mail: sunando.patra@gmail.com

^de-mail: roy.satya05@gmail.com

Different types of neural networks have been developed over the last couple of decades, each tailor-made to embed input tensors of a specific type. While a Convolutional neural network (CNN) uses $2D$ convolutions on an image to do this, a recurrent neural network (RNN) is best suited for data presented as sequences, e.g., audio files, time series, and natural language; a graph neural network (GNN) works best on data with distinct global, node/vertex, and edge features, and so on. These models vary widely in their architectures, with completely different workflows. As one type of data can be represented in multiple ways, these models can be applied independently to them with varying performance measures. For example, pixels of a colored digital image can be represented as vectors, multi-channel $2D$ tensors, graphs, or even fixed-length point clouds. Historically, the calorimeter energy deposits of the constituent particles in a jet were first represented as a $2D$ image/grid, with pixel intensity representing their respective energy/ p_T , making CNNs—followed by a dense/linear network (colloquially known as multi-layer perceptrons or MLPs)—the default networks for jet-embedding and subsequent classification [32–39].

A more direct approach to embedding is to represent the jet as a point cloud of its constituent particles. Each ‘point’ is a particle with its own set of features, e.g., four momentum components, particle IDs, charges, and tracking information. GNNs [40–42] are particularly well-suited for this representation. The jet is now treated as a graph where each particle is a ‘node’, and the connections between them are ‘edges’ [43–49]. Constituent information can also be represented as a varying length sequence, especially if it is ordered based on a certain property, e.g., by their transverse momentum p_T . RNNs—originally developed for processing text or speech—can then be used. The advent of the self- and cross-attention mechanisms gave us the famously parallelizable and scalable *Transformer* architecture [50]. Originally used to process and generate natural language sequences, these models can be thought of as special variations of GNNs [51], and can process jets either as sequences of constituents or unordered point clouds.

One jarring issue that plagues the existing networks with the highest accuracy in identifying various jets is the computational cost. Achieving high accuracy boils down to extracting maximal information from the jet representation. It can either be gleaned by formidably large networks or can be preprocessed and fed to a smaller network later. The former is the path taken by transformer-based models [52–54] and more costly foundational models like *Omnilearn(ed)* [18, 55, 56]. Even these, when striving for higher accuracies, bring separately extracted features to the networks ‘at-

tention’¹. In the latter approach, when jets are considered as particle clouds or graphs, creating a fully connected graph is prohibitively costly in terms of time and computation, mainly because the pairwise interactions (edge information²) are numerous for a jet with a large number of constituents. These challenges are either bypassed by keeping only the nearest neighbor interactions (*ParticleNet* [44]), or by representing data in a geometric algebra over space-time, equivariant under physics-motivated (Lorentz) transformations [46–48]. The newer architectures combine both of these approaches [57, 58]. Even running these state-of-the-art models on single-GPU machines becomes an ordeal, let alone training them from scratch. With the rising awareness of the virtues of Transfer Learning, more models are now pre-trained on larger datasets with multiple classes, which automatically requires significant model complexity. This considerably increases their performance, but the downside is that the cost of re-training increases many times over for specific downstream tasks.

Our objective in this work is to revisit computationally low-cost CNNs, as they implicitly utilize local, pairwise information (albeit spatially, through images) to some extent. Depending on the knowledge that the inclusion of global jet features enhances tagging efficiency [17], we explore the possibility of constructing a lightweight yet efficient network by incorporating global features with the images. Although computationally lightweight, smaller CNNs such as LeNet [59] cannot achieve competitive accuracies. Extracting more information here is equivalent to increasing image resolution and/or model complexity (depth/width). Although CNNs become notoriously computationally costly when scaled up (e.g., ResNet [60]), recent developments, such as compound scaling [61, 62], combined with depthwise and pointwise convolutions [63–67], resulted in networks that reach higher accuracies at a fraction of the cost. As all versions of *EfficientNet* were originally designed for images with higher resolution, we have built lightweight versions of those, while following the same scaling rules. We aim to explore their capabilities with and without the externally provided global features, while using LeNet as a benchmark for comparison throughout.

The paper is organized as follows. In Section 2 we provide a detailed account of our methodology. This includes machine configuration, training data preparation, model architectures, and training procedure. In Section 3 we present our results. Finally, in Section 4, we summarize our work and draw conclusions.

¹Not adding pairwise information to the multi-head attention of the (*Par-T*) network results in a 1.2% drop in accuracy and a 20 – 30% drop in background rejection [44, 52].

²i.e., the abstract message-passing, not physical QCD interactions.

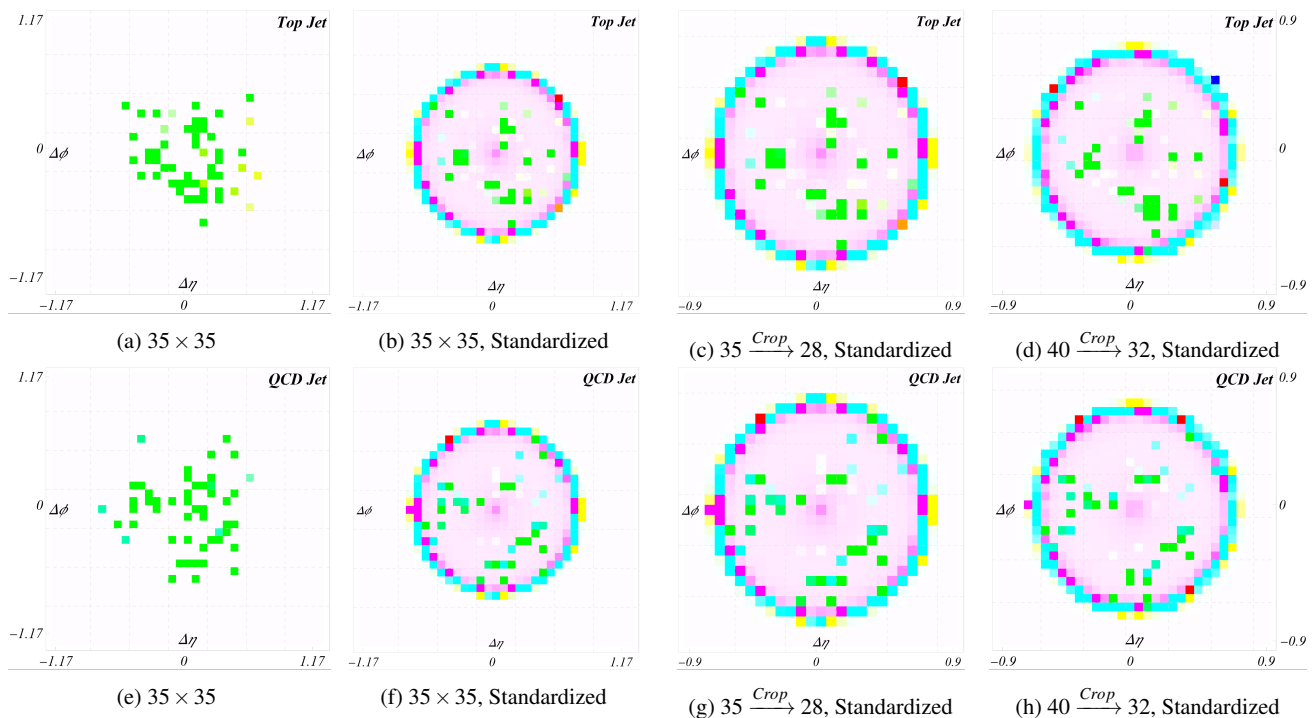


Fig. 1: Representative images of two jets for different resolutions and pixel standardization. Although images in our dataset are rendered in RGB, we present them here using the CEI 1931 XYZ color scheme [68], for better visual understanding. All images from the top panel are of one representative top jet, and those below are of one QCD jet. The first column shows the jet constituents as a 35×35 image in the $\Delta\eta - \Delta\phi$ plane, as the channels are combined and rendered. The second panel in the same row contains the same image, with the pixels standardized (the mean image of the dataset is subtracted from the original and then divided by the standard deviation image). The third column displays the images in the second, but cropped to 28×28 . The fourth column contains the same jets, first rendered in 40×40 , then cropped to 32×32 .

2 Methodology

2.1 Machine Configuration

All training and measurements, except for the measurement of inference speed, are performed on a single desktop PC with 64GB RAM, a 13th generation Intel[®] i9 processor, and a 12GB NVIDIA[®] RTX A2000 graphics processor. The entire analysis is conducted in Mathematica[®] with the Wolfram Language, which uses the Apache MXNet[®] framework in the backend. The original EfficientNet architectures (before modification) were taken from the Wolfram Net Repository [69]. To compare the inference speed of CNNs in this work with some external models, inference times were calculated on another machine with an 11GB NVIDIA[®] GeForce GTX 1080-Ti graphics processor.

2.2 Data: Images from Constituents

We have used a pre-existing dataset³ that contains both top-quark and mixed light-quark-gluon jets. The objective, as mentioned before, is to identify top quark jets as signals and

³<https://syncandshare.desy.de/public.php/dav/files/11bX3zpLhazgPJ6/?accept=zip>

tag them as fat jets amid the sea of other jets. The events were generated with 14 TeV center-of-mass energy using Pythia8 [70] followed by detector simulation performed using Delphes [71]. The jets were constructed using the anti-kT algorithm [72] with FastJet [73]. The pseudorapidity $|\eta_j|$ is required to be < 2 for the fat top quark jet, whereas the radius parameter is chosen to be 0.8. It is ensured that a matched parton-level top exists within $\Delta R = 0.8$ of this signal jet. Moreover, all decay products of the top quark are required to be within $\Delta R = 0.8$ of the jet axis. 4-momenta information is stored for the leading 200 jet constituents. The leading top-quark jets lie within a p_T range of 550 – 650 GeV. The total sample consists of one million top jets alongside another million non-top jets, which are treated here as background. The dataset is divided into training / validation / test (1.2M/0.4M/0.4M) sets.

We pre-process the data to create 3-channel images with transverse momentum (p_T), mass (m), and energy (E) in each channel, respectively. To create each channel from the jet constituents, the hardest constituent is considered to be the center of the channel, and the rest of the image is constructed by binning the remaining constituents in two dimensions: the difference in pseudo-rapidity ($\Delta\eta$) and that in the azimuthal angle ($\Delta\phi$). The paper associated with the

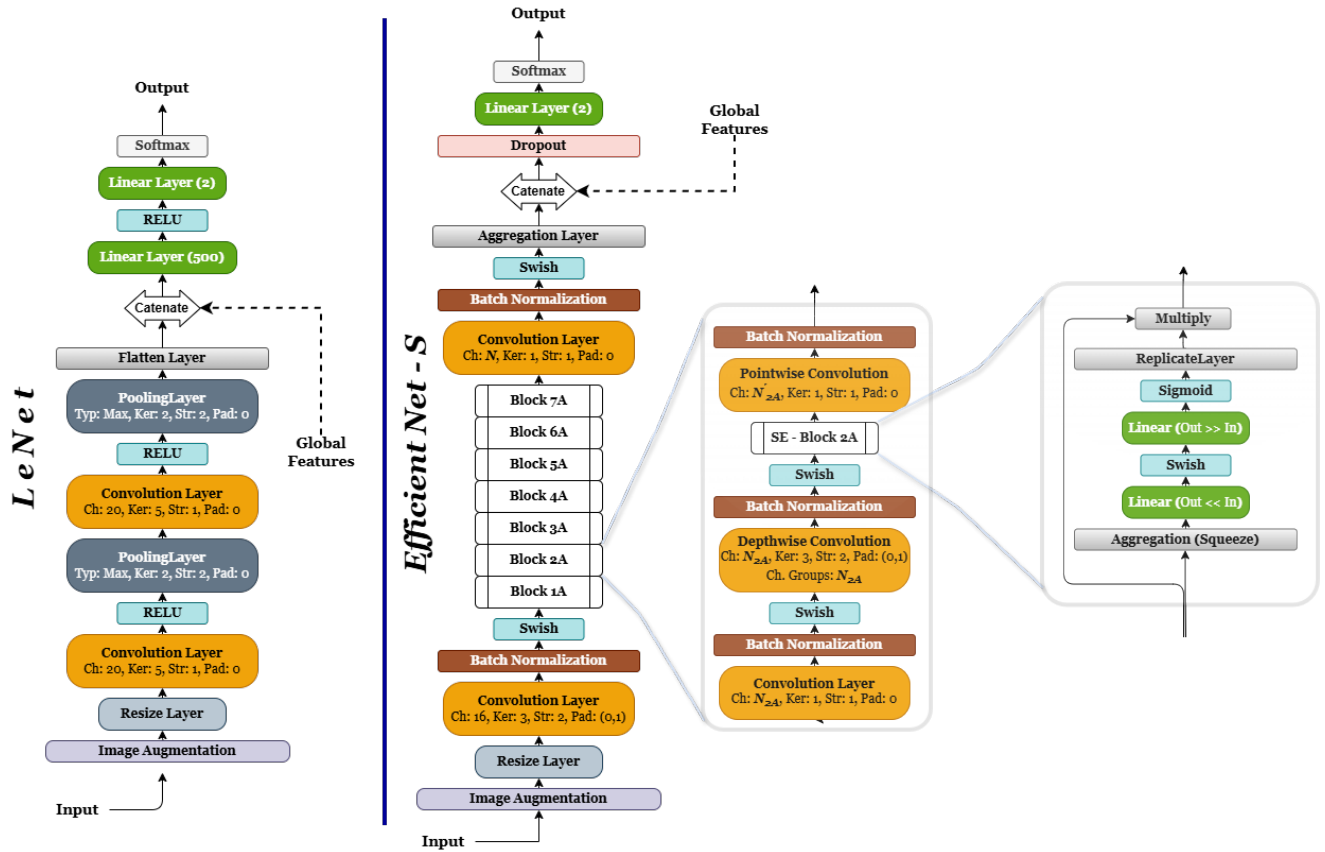


Fig. 2: Schematics of network architectures used in this work. On the left is *LeNet*, used as the benchmark CNN model. On the Right is the simplest Efficient Net (small) used. Representative schematics of the *M-Conv* blocks and the squeeze and expand residual blocks within those are also shown.

original dataset [36] assumes the calorimeter resolution to be $0.04 \times 2.25^\circ$, where a fat jet with a radius parameter $R = 0.8$ can be covered with 40×40 pixels. Both $\Delta\eta$ and $\Delta\phi$ axes are retained from -1.2 to 1.2 for this dataset, without the loss of any constituents. We keep more of the field of images than is usual practice in the community, where final images are generally cropped to $R = 0.8$ [34–36]; our images are center-cropped at $R = 0.96$. To keep the images as small as possible, we use two sizes in the course of this work: 35×35 (see Figs (1a) and (1e)) and 40×40 . In the original paper, the axis of the image is rotated in such a way that the second hardest p_T object falls on the positive $\Delta\phi$ axis and the third hardest constituent in the first quadrant. We have found out that this results in a lower accuracy for classification; rather, we use an image augmentation layer to randomly flip the image along either axis or both during training. We do not use random cropping, as the jets are constructed objects and can—for all practical applications—be centered around the hardest p_T constituent. Furthermore, to use *N-subjettiness* later in our analysis, we also require each jet to have at least 4 constituents, which drops a meager 33 jets from the 201.8K dataset.

Standardization of input data has become common in ML, as it has been found to improve the performance of generic neural networks. We perform this standardization by creating a ‘mean’ and a ‘standard deviation’ image using a large number of random samples from the dataset. We respectively subtract from and divide every sample by the values of these arrays. This clearly isolates a fairly circular region in the $\Delta\eta - \Delta\phi$ plane containing the bulk of the jet structure (see Figs (1b) and (1f)). Thus, we apply a center-crop to the 35×35 images, making them 28×28 ($R \sim 0.96$, see Figs (1c) and (1g)). A similar size of the central region is obtained for the 40×40 images when they are cropped to 32×32 (see Figs (1d) and (1h)).

2.3 Data: Jet-Level Information

We have combined some global features of the jet to ascertain how much they improve the tagging efficiency of the CNNs. The features used in this work are inspired by ref.s [17, 74]. The original dataset provides the four-momentum of up to 200 constituents per jet, from which all global features can be computed. For this purpose, we employ the

fastjet package along with EnergyCorrelator contrib from fastjet-contrib-1.3.2.

In addition to the global four-momentum of the jet, our feature set includes the N -subjettiness variables [19], as well as several series of observables constructed from Energy Correlation Functions [22] and generalized correlator functions [23]. The complete list of variables is as follows:

- Jet four-momentum: $p_T, \eta, \phi, m_{\text{jet}}$
- Number of constituents: N_{cons}
- N -subjettiness ratios: $\tau_{21}^\beta, \tau_{32}^\beta, \tau_{43}^\beta, \tau_{54}^\beta, \tau_{65}^\beta$ for $\beta = 0.5, 1.0, 2.0$
- C -series: $C_1^\beta, C_2^\beta, C_3^\beta$ for $\beta = 1.0, 2.0$
- D -series⁴: $D_2^{\alpha,\beta}$ for $\alpha, \beta = 1.0, 2.0$, and the four D_3 variables defined in [17]
- U -series: $U_1^\beta, U_2^\beta, U_3^\beta$ for $\beta = 0.5, 1.0, 2.0$
- M -series: M_2^β, M_3^β for $\beta = 1.0, 2.0$
- N -series: N_2^β, N_3^β for $\beta = 1.0, 2.0$
- L -series: L_2, L_3 as defined in [74]

Certain global features, such as U_3^β and M_3^β , require at least 4 constituents for their computation. As mentioned in the previous sub-section, we discard all jets with $N_{\text{constituents}} < 4$. For complete definitions and a detailed description of these variables, we refer the reader to ref.s [17, 74]

2.4 Model Architecture

Historically, one of the most successful convolutional neural networks (CNNs), *LeNet* [59], is also the oldest and one of the simplest. *LeNet-5*, with alternating convolutional and pooling layers, has been the dependable standard for smaller images (see the left side of Fig. (2) for its architecture). Over the decades following *LeNet*, CNNs continued to scale up to classify images at increasingly higher resolutions. AlexNet [78], Inception nets [79, 80], ResNets [60] and their wider versions [81], DenseNets [82], and MobileNets [63–66] are only a few examples of these. To go deeper and wider, these newer architectures used varied techniques, such as ‘residual’ connections to feed information from earlier layers to the latter parts of the network, point-wise (1×1) and depth-wise convolutions for dimension reduction to remove computational bottlenecks, batch normalization, and mixtures of these methods [83, 84]. Targeting general-purpose image classification, these models were optimized for the ImageNet dataset [85, 86] and its equivalents; thus, computationally, they are quite expensive.

Though scaling CNNs according to image resolution has been attempted before [87], EfficientNets [61, 62] were the first to solve the scaling problem by using ‘compound scaling’, connecting network *depth* and *width* to image *resolu-*

⁴The parameter choices for the D -series features follow [75–77].

Layers	Input Resolution	
	$3 \times 40 \times 40$	$3 \times 64 \times 64$
Conv 3×3	$16 \times 20 \times 20$	$16 \times 32 \times 32$
Block 1A	$8 \times 20 \times 20$	$8 \times 32 \times 32$
Block 2A	$8 \times 10 \times 10$	$16 \times 16 \times 16$
Block 3A	$16 \times 5 \times 5$	$16 \times 8 \times 8$
Block 4A	$24 \times 3 \times 3$	$32 \times 4 \times 4$
Block 5A	$32 \times 3 \times 3$	$48 \times 4 \times 4$
Block 6A	$56 \times 2 \times 2$	$80 \times 2 \times 2$
Block 7A	$96 \times 2 \times 2$	$136 \times 2 \times 2$
Conv 3×3	$400 \times 2 \times 2$	$536 \times 2 \times 2$
Aggregate	400	536
FC & Out	2	2

Table 1: *Effnet-S* configurations for two different input resolutions. For more details, see sec. 2.4.

tion. Given a baseline network (found from a neural architecture search, or NAS), these quantities scale as:

$$\begin{aligned}
 \text{depth coefficient } d &= \alpha^\phi \\
 \text{width coefficient } w &= \beta^\phi \\
 \text{resolution coefficient } r &= \gamma^\phi,
 \end{aligned} \tag{1}$$

where $\alpha \geq 1, \beta \geq 1, \gamma \geq 1$. Here, increasing ϕ , the scaling parameter, increases the complexity of the network in a compounded manner. Noting that doubling the net-depth doubles the computational cost (floating point operations per second, or FLOPS), but doubling the other two quadruples the FLOPS, these also follow an empirical constraint: $\alpha \cdot \beta^2 \cdot \gamma^2 \simeq 2$, so that increasing ϕ by some ϕ_0 increases the FLOPS by 2^{ϕ_0} . The authors of the first EfficientNet paper performed a grid search on α, β , and γ and obtained the values 1.2, 1.1, and 1.15, respectively. Starting with $\phi = 0$ and increasing ϕ by 1 each time, they obtained eight networks (B_0 to B_7) with increasing complexity. The base network (B_0) works on arrays of dimension 224×224 , while the largest of these models (B_7) takes in arrays of dimension 600×600 . There are seven main building blocks of an EfficientNet, each containing multiple parts. Building upon other successful lightweight models [64, 67], EfficientNets replace a fully convolutional operation with a depthwise convolution (a single filter per channel) and a pointwise (1×1) convolution (see the blown up schematic of *Block 2A* in Fig. (2)). This significantly reduces the computational cost while maintaining similar performance. When stacked together, the blocks mentioned above also perform a function known as inverted bottlenecking, embedding the input manifold into a lower-dimensional manifold. Each of these blocks also contains a *squeeze and expansion* block [88],

Network Type	Input Array ($3 \times n \times n$)	Img. Res. ($Org \rightarrow Crp$)	No. of Param.s Param.s	Inference Time (ms) /100 Jets	Accuracy (%)		AUC		Bkg. Rejection at TPR	
					Avg.	Best	Avg.	Best	50%	30%
<i>LeNet</i> (Images)	28	35 \rightarrow 28	428K	5.7(8)	92.42(3)	92.48	97.74(1)	97.76	156(2)	480(18)
	32		653K	6.1(9)	92.40(2)	92.43	97.74(1)	97.74	154(3)	483(13)
	40		1253K	6.4(8)	92.45(3)	92.50	97.76(2)	97.78	161(4)	514(23)
	32	40 \rightarrow 32	653K	11.9(10)	92.41(4)	92.48	97.75(1)	97.76	161(3)	512(25)
	40		1253K	13.4(18)	92.42(5)	92.48	97.74(1)	97.74	154(3)	476(11)
(Images + Global Feat.s)	28	35 \rightarrow 28	485K	5.7(8)	93.33(2)	93.37	98.24(0)	98.24	258(5)	916(25)
	32		710K	6.1(8)	93.34(2)	93.38	98.24(1)	98.26	257(3)	942(31)
	40		1310K	6.6(9)	93.31(3)	93.36	98.23(1)	98.25	255(5)	909(34)
	32	40 \rightarrow 32	710K	14.5(16)	93.33(2)	93.36	98.24(0)	98.24	255(2)	951(43)
	40		1310K	14.8(7)	93.34(2)	93.37	98.24(1)	98.25	263(3)	906(32)
<i>EffNet-S</i> (Images)	36 (<i>S0</i>)	35 \rightarrow 28	158K	7.3(9)	92.31(11)	92.50	97.73(4)	97.80	160(5)	536(24)
	40 (<i>S1</i>)		184K	8.0(7)	92.35(8)	92.46	97.75(3)	97.76	163(3)	552(18)
	48 (<i>S2</i>)		215K	8.7(8)	92.39(9)	92.53	97.76(4)	97.80	167(5)	569(30)
	56 (<i>S3</i>)		258K	9.6(8)	92.58(1)	92.72	97.85(3)	97.90	171(6)	585(32)
	64 (<i>S4</i>)		305K	10.6(8)	92.20(40)	92.75	97.74(11)	97.92	156(16)	499(78)
	36 (<i>S0</i>)	40 \rightarrow 32	158K	13.5(10)	91.40(60)	91.91	97.37(13)	97.50	127(11)	431(49)
	40 (<i>S1</i>)		184K	13.9(10)	90.5(12)	91.80	97.22(26)	97.39	112(15)	361(57)
	48 (<i>S2</i>)		215K	14.8(10)	91.4(10)	92.05	97.35(23)	97.56	126(18)	407(64)
	56 (<i>S3</i>)		258K	15.8(7)	92.0(4)	92.31	97.60(10)	97.68	143(9)	460(45)
	64 (<i>S4</i>)		305K	16.5(9)	91.9(6)	92.42	97.52(18)	97.74	137(17)	434(63)
(Img.s + Glob. Feat.s)	36 (<i>S0</i>)	35 \rightarrow 28	242K	8.2(9)	93.28(2)	93.32	98.21(1)	98.23	242(5)	890(34)
	40 (<i>S1</i>)		276K	7.9(9)	93.26(2)	93.30	98.21(1)	98.22	241(7)	859(34)
	48 (<i>S2</i>)		315K	8.4(9)	93.20(2)	93.30	98.18(2)	98.20	241(10)	839(51)
	56 (<i>S3</i>)		368K	10.0(10)	93.31(5)	93.38	98.21(1)	98.22	232(5)	817(26)
	64 (<i>S4</i>)		422K	11.4(9)	93.15(5)	93.24	98.11(3)	98.15	208(8)	707(48)
	36 (<i>S0</i>)	40 \rightarrow 32	242K	13.8(8)	93.24(8)	93.31	98.20(4)	98.23	244(13)	897(74)
	40 (<i>S1</i>)		276K	13.6(12)	93.26(2)	93.31	98.20(1)	98.21	247(6)	868(25)
	48 (<i>S2</i>)		315K	14.4(9)	93.20(3)	93.26	98.17(2)	98.20	235(6)	864(30)
	56 (<i>S3</i>)		368K	15.7(9)	93.22(9)	93.35	98.18(3)	98.23	237(9)	829(44)
64 (<i>S4</i>)	422K	17.0(10)	93.21(5)	93.27	98.15(3)	98.18	225(13)	778(71)		
DeepTop [34–36]	1 \times 37 \times 37	60 \rightarrow 40 \rightarrow 37	610K	–	–	93.00	–	98.10	–	914(14)
ResNeXt-50 [84]										
Ref. [36]	1 \times 64 \times 64	96 \rightarrow 64	1460K	–	–	93.60	–	98.40	–	1122(47)
Ref. [44]	1 \times 64 \times 64	96 \rightarrow 64	1460K	22	–	93.60	–	98.37	302(5)	1147(58)

Table 2: Single number performance metrics for ML models performed on the total test dataset. From the second to the seventh column, we respectively report the input array sizes, the resolution of the generated jet images ($A \rightarrow B$ means the original image was $A \times A$, and it was cropped to $B \times B$), total number of parameters in the network, inference time for 100 jets in milliseconds, overall accuracy, and area under the ROC curve (AUC). The last two columns list the QCD background rejection at top tagging efficiencies of 50% and 30%, respectively. The values in bold-face represent the best metrics for a specific type of Network.

with a residual connection maintaining the information flow, as well as a combination of *Swish*, *RELU*, and *Sigmoid* activation functions. More details can be found in the original paper [61]. While the width coefficient scales up the channel dimension of each block, the depth coefficient determines

the number of times each type of block is repeated, making the network deeper. These networks also scale up the dropout probability to regularize the larger models. All versions of EfficientNet outperform other CNNs that are much larger in size (in terms of accuracy) while being faster dur-

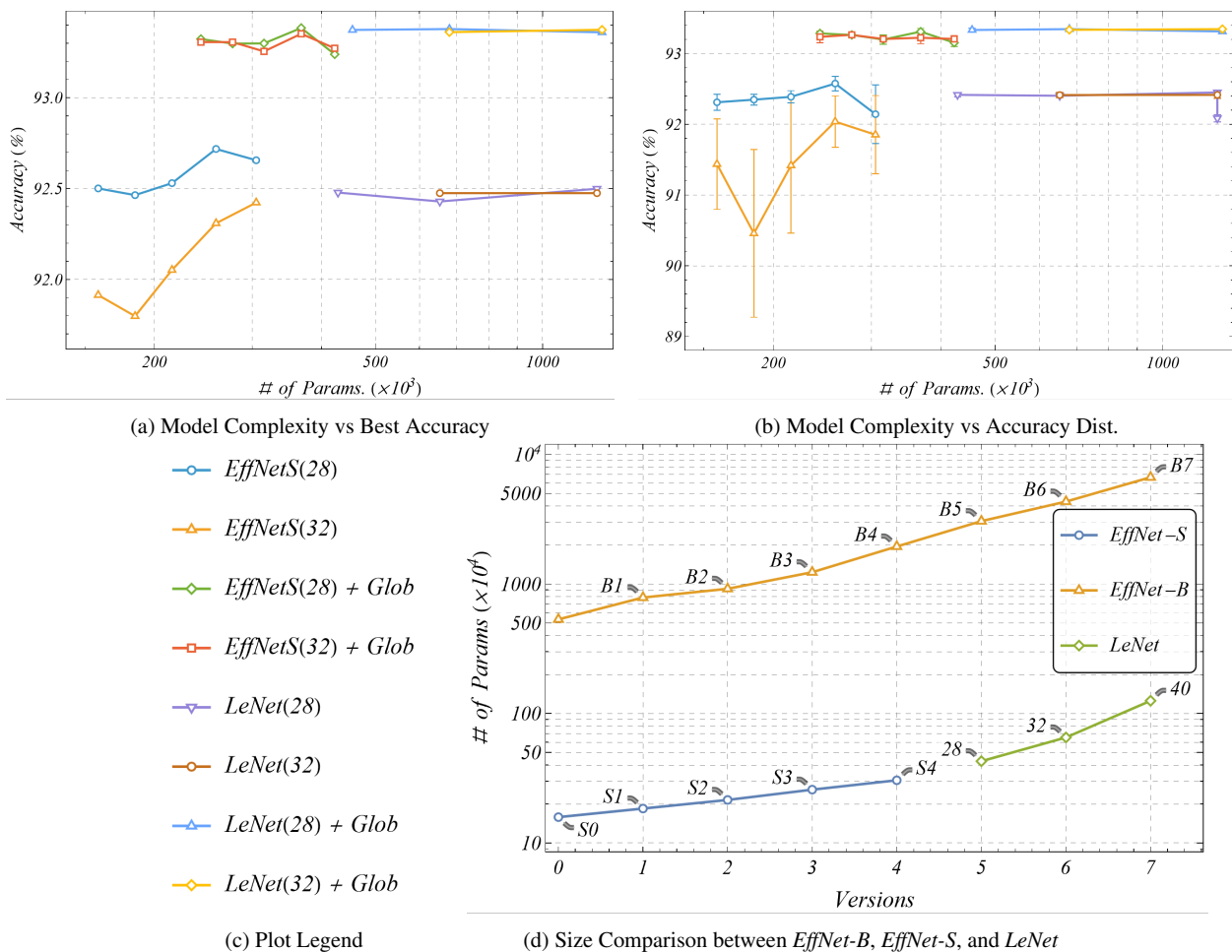


Fig. 3: Performance comparison of different CNN architectures: fig. (a) shows the best accuracies vs. number of model parameters of the nets used, fig. (b) shows the median accuracies and error-bars in the same setting, fig. (c) is the legend for (a) and (b), and fig. (d) is a comparison of sizes of the networks compared to traditional *EfficientNet* versions.

ing inference (B_0 , with 5.3 M parameters, achieves a top-5 accuracy of 93.3% for ImageNet, compared to the widely used ResNet-50 (26 M parameters)—which has a top-5 accuracy of 93.0%; the FLOPS for ResNet-50 is 11 times that of *EfficientNet-B_0*).

We begin with *LeNet* in this analysis as a benchmark for performance. Following its historical usage, the smallest resolution of jet images we use is 28×28 , increasing to 32×32 and 40×40 . Images larger than these make the jet constituents sparser, and CNNs with even higher-resolution inputs are needed for their analysis. The network we focus on here is *EfficientNet*. While they have been used on smaller images, such as the CIFAR-10 and CIFAR-100 datasets, these have been upsampled to fit the 224×224 input dimensions⁵. This defeats one of the main purposes of this work (working with constrained computational resources), both in terms of RAM and VRAM.

To circumvent this without changing the hyperparameters of the original *EfficientNet* architecture (and using the prescribed values of α , β , and γ), we use negative ϕ values to scale down the input resolution. The smallest resolution thus achieved is 36×36 . Any smaller, and the bottlenecks within the network would not hold without modification. We choose the starting resolution to be 36×36 , corresponding to $\phi = -13$, then repeatedly increase ϕ by 1 to get the rest of the configurations. We thus create 5 variants, the last one corresponding to $\phi = -9$ ⁶. The other important parameter to set is the dropout probability, which is gradually increased from B_0 to B_7 , as more regularization is needed for larger networks. We linearly extrapolated these values using the width and depth coefficients and found that for input array widths < 90 , we do not need dropouts. Altogether, we will denote this smaller architecture as *EfficientNet-Small* (*EffNet-S*) for this work. For these values of ϕ , every block

⁵Author’s answer: <https://github.com/tensorflow/tpu/issues/421>.

⁶Similar efforts can be found here: <https://github.com/qubvel/efficientnet/issues/26>

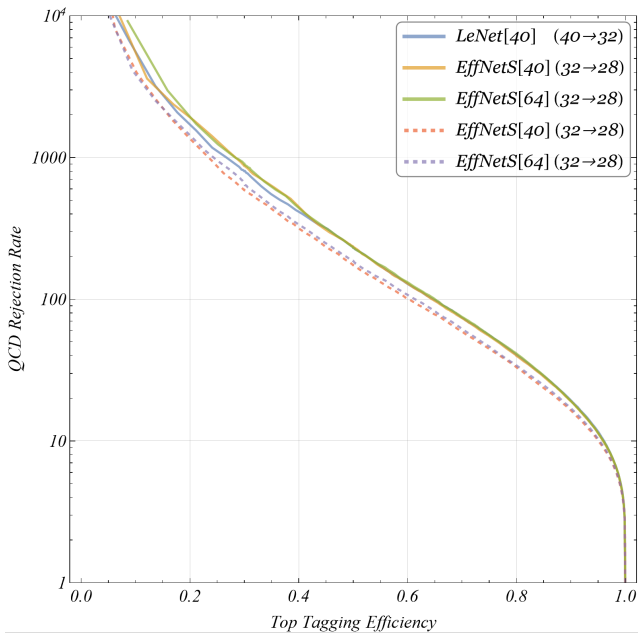


Fig. 4: ROC curve (signal efficiency vs. background rejection) for some of the networks (with some metric highest among others; table (2) has them in bold-face). The solid lines are for models working on both images and global features, dashed ones correspond to those with only images as input. The solid black curve is the optimal ROC curve obtainable by any model, obtained from *likelihood ratio* analysis (ref. [?]).

appears only once in the smaller *EffNet-S* structures. We have thus indexed the blocks ‘*i-A*’ ($i = 1, 2, \dots$), to keep the possibility of larger networks open⁷. Table (1) lists the input dimensions for this architecture for two different input resolutions: 40×40 and 64×64 .

2.5 Training

Although we load the validation and test datasets into RAM as a whole, due to our choice of confining ourselves to a single mid-range PC with 64GB RAM, we use a type of data piping for the training dataset. We load 300,000 training data at a time, which we will call a ‘*round*’ from now on. Each round is trained until the validation loss stops decreasing for 10 epochs. An image of the trained network is saved from each round and used in the next one. This is done for 12 rounds for 35×35 (40×40) image representation of jets to ensure that the entire dataset is adequately represented.

⁷This raises an obvious question: as these CNNs were fine-tuned to detect specific *shapes* (with detail) from larger images, unlike in our case—where the jet-images are smaller and are mere representations with a much larger importance to finer structures—could it be possible to systematically search for and create versions of scalable networks for this specific task, albeit smaller? Though intriguing, this question is outside the scope of the present work. However, glimpses of this possibility may be perceived from the present analysis.

For most of the models used in this work, we repeat the process, starting with the last trained network, and use the same rounds again. This way, the rounds mimic the behavior of epochs, while storing the datasets in advance reduces computation time. We then evaluate the accuracy of each model on the test dataset, and the model with the highest accuracy is saved as the best version of that specific architecture. All further measurements are performed on this iteration of the model.

To ensure optimal computation time, we choose batch sizes depending on whether the memory dedicated to the graphics card can handle them without overflowing into the SWAP memory. For *EffNet-S* versions 0, 1, and 2, a batch size of 4096 is used; for *EffNet-S* versions 3 and 4, these numbers are respectively 3072 and 2560. For all other networks, it is fixed at 4096. We use the *ADAM* optimizer [89] with default settings ($\beta_1 = 0.9$, $\beta_2 = 0.99$, and $\epsilon = 10^{-5}$, along with the default learning rate update schedule) to minimize the cross-entropy loss, where we wait for a fixed number of *epochs* (generally 10) for the last minimum loss to be updated; otherwise, we stop the training.

The global features of the jets are standardized and utilized in the second part of the analysis, in conjunction with the images. These are concatenated with the output of the ‘*Flatten Layer*’ of *LeNet* and, in the case of *EffNet-S*, that of the ‘*Aggregation Layer*’, as can be seen from Fig. (2). Pre-trained networks are faster to retrain and reach higher accuracies after modification—a fact that has been re-established in recent attempts at foundational models in jet applications. Keeping that in mind, we use the first part of the best network of a particular architecture and add an MLP block to it in this part of the analysis.

We retrain the best network of each architecture 9 additional times, with a representative subset of the dataset, to obtain the uncertainties arising from random weight initialization.

3 Results

Table (2) lists all single-number performance metrics for the networks explored in this analysis. The table is divided into three blocks: the first block contains all the information about the *LeNet* architecture, the second one about *EffNet-S*, and the third one lists some of the publicly available information about CNNs used previously as top-taggers for comparison. We have obtained results for *LeNet*-type networks with three two different input resolutions: 35×35 , and 40×40 . Versions of *EffNet-S* are of 5 types: 0 to 4. Images are generated in two ways: 35×35 images cropped to 28×28 and 40×40 images cropped to 32×32 , as explained in sec. 2.2. Each network is run on all images with cropped resolution (col. 3 of tab. 2) less than or equal to its input dimension (col. 2 of tab. 2). Networks with a specific architec-

ture and input resolution optimized for maximum accuracy are used to create versions that can also process the global features.

LeNets with increasing input array-sizes, when applied only to images cropped to 28×28 , gain marginally in performance across all metrics. Incorporating global features clearly increases the discriminative power—especially background rejection—of the networks, and the effect is more prominent for higher image resolutions. This is expected, as *LeNet* is a conventional CNN. Full convolutions with a large kernel size (5) extract more information from the images, albeit at a higher computational cost and a heavier network. The *LeNet-40* is 2.9(2.7) times the size of *LeNet-40* without(with) global features.

The smallest *EffNet-S*, while applied only to images, achieves accuracy similar to the largest *LeNet*, while being 1/8-th in size (the total number of parameters). Its performance is best when the input images are $35 \xrightarrow{\text{Crop}} 28$, but it drops quite a lot for the larger images. Adding global features is beneficial here as well, but the effect is less prominent for larger networks. We have shown the best metrics in each column in bold-face, for both the cases with and without global features.

As was mentioned earlier in sec. 2.1, the inference timings were calculated in a separate machine with a weaker GPU. While networks consistently take more time for larger image sizes, all of the networks dealt with in this work have almost half the inference time of that of *ResNeXt-50*.

Fig. (3) summarizes the accuracies of table (2) in comparison to architecture complexity (number of net-parameters). Fig. (3d) shows the relative sizes of different versions of *EffNet-S* compared to the versions of *LeNets* used in this analysis as well as the larger and standard *EfficientNets* (*B0* to *B7*), where the number of parameters is in log-scale. Even the largest *EffNet-S* is smaller than the smallest *LeNet* and all of these are an order of magnitude smaller than *EffNet-Bs*. In figures (3a) and (3b), accuracies of the nets are compared, with their model complexity in the x -axis. While fig. (3a) plots the best accuracies for each type of net, fig. (3b) shows the variation in it arising from random weight initialization. These employ 10 runs each, as mentioned at the end of the last section.

As far as accuracies are concerned and for only images as input, we see that the performance of *LeNet* does not change much (and remains within randomization error), with increasing complexity, for all image resolutions. The *EffNet-S*, on the other hand, performs worse for larger image sizes. For the larger variants, this loss in performance falls within the randomization error-bar, but overall, the performance not only worsens, but has larger variance for $40 \xrightarrow{\text{Crop}} 32$ images. The possible reason is that the ‘MB-Conv’ blocks with bottlenecks in *EffNet-S* do not perform at the level of full convo-

lutions when analyzing sparse pixel-level information, and networks with larger input arrays are needed for proper classification.

While the addition of global features improves network performances by a margin, the accuracies become more or less independent of the network complexity across architectures, especially when randomization errors are considered. One possibility is that the extra MLP block after the last Aggregation layer contributes far less than the rest of the network, but the more probable explanation would be that the impact of global features overshadow the CNN-performance. Analyzing higher input sizes and higher image resolutions can shed more light on this. More work is needed regarding the integration of the global features in these networks.

Fig. (4) shows the signal (top) efficiency vs. the background (QCD) rejection curves for those representative models for which at least one of the metrics is highest among others (those in bold-face in table 2). This also shows how all *EffNet-S* nets outperform the best *LeNet* with just images as input (dashed curves), but with Global features put in, all of their performances are equivalent (solid, colored curves). We have also added the optimal possible ROC curve obtained from *likelihood ratio* analysis using generative models (ref. [?]; in thick black) to showcase the space allowed for future progress.

In the case of other CNNs, the entries for the ‘Image Resolution’ column are calculated in the following way: we know these images were created 40×40 (*DeepTop*) and 64×64 (for *ResNext*) for $R = 0.8$. This corresponds to 60×60 and 96×96 for $R = 1.2$, which is our case. These are all grayscale images with only one channel for p_T . All networks used in this analysis that utilize the global features outperform the classic *DeepTop* CNN structure in terms of accuracy, if not in background rejection. *ResNeXt-50* has a much better performance, but it is considerably heavier than the *EffNet-S* (the best performing global feat. variant is 1/7-th in size of *ResNeXt-50*). These nets are faster as well. The longest inference time for *EffNet-S* is half of that for *ResNeXt-50*.

4 Conclusion

Jet tagging, a classification problem that aims to identify jets originating from different particles (top quarks, Higgs boson, gauge bosons, light quarks, or gluons), remains a challenging, albeit one of the most important tasks, especially in the context of a hadron collider like the LHC. Machine learning has now replaced traditional use of hand-crafted features to become an integral part of jet physics studies. Depending on the network used, jets are treated as images, sequences, trees or graphs. Existing literature shows

that transformer-based networks, which treat jets as particle clouds or graphs, perform the best. To achieve the highest possible accuracy, incorporating pairwise information is crucial. However, given the large number of pairwise interactions among the constituents of a jet, creating a fully connected graph becomes a computationally costly affair. CNNs, on the other hand, while being computationally low-cost, treat jets as images/arrays denoting the spatial arrangement of constituent particles in terms of energy, momentum, and mass; thus can utilize at least some local pairwise information. One can additionally incorporate global features of the jets to either directly to the images or to the network to enhance the jet identification accuracy. We have explored the possibility of combining these features and construct a computationally lightweight but efficient CNN-based network that can compete with other similar architectures.

With traditional CNNs, larger/deeper networks are needed to extract maximal information from the jet images, as opposed to typically lightweight CNNs like *LeNet*. Scaled-up CNNs, such as *ResNets* are computationally costly. Using recent advancements in the construction of CNNs, we have used lightweight versions of *EfficientNet* to circumvent this issue. Although these were built to work on higher resolution images, one can follow a set of prescribed scaling rules to construct a network applicable for low resolution jet images as well. We have performed a comparative study with and without externally provided global features. Results for *LeNet* are also provided as a benchmark for comparison.

We observe that adding global features to the models, along with the images, results in better accuracy. Although this the increase in performance is somewhat monotonic with increasing image resolution for fully convolutional models, such as *LeNet*, the corresponding relationship for *EffNet-S* is not so straightforward; increasing the input array size also improves the overall performance. The performance of these models becomes somewhat independent of their architecture in the presence of the global features. When applied to jet-classification tasks, this begs for further inquiry into the interplay between global features and constituent-level information.

This exploration leads to three observations: *first*, there needs to be a systematic architecture search for versions of scalable models such as *EfficientNet*, tuned for jet classification; *second*, adding global jet features, in addition to the constituent information, makes it easier for smaller models to perform better, but the exact way these features are fed-in needs further exploration; *last but not least*, as jets can have multiple types of representation, e.g., image, constituent four-momenta, and global jet features, one can combine the strengths of different network architectures and build a hybrid ‘mixture of experts’ ensemble of lightweight networks with the potential for superior performance, leading to better signal-to-background discrimination. Exploring these

ideas is beyond the scope of this paper, but it is something that we plan to work on as a subsequent project.

Acknowledgements RB, SM, and SKP would like to acknowledge support from ANRF, India (grant order no. CRG/2022/003208). SM would also like to acknowledge ANRF for grant order no. CRG/2023/008570.

References

1. S. Yang, Y.-H. Wang, P.-B. Zhao, and J.-L. Ma, “Searching for heavy vector-like B quark via pair production in fully hadronic channels at the CLIC,” [arXiv:2504.15882 \[hep-ph\]](#).
2. A. Ghosh, S. Ghosh, S. Mitra, T. Samui, and R. K. Singh, “Improving Sensitivity of Vector-like Top Partner Searches with Jet Substructure,” [arXiv:2507.03199 \[hep-ph\]](#).
3. D. Sahoo, R. Sahu, and K. Ghosh, “A Comprehensive Search for Leptoquarks Decaying into Top- τ Final States at the Future LHC,” [arXiv:2501.07543 \[hep-ph\]](#).
4. A. Bhaskar and M. Mitra, “Boosted top quark inspired leptoquark searches at the muon collider,” *Phys. Lett. B* **868** (2025) 139656, [arXiv:2409.15992 \[hep-ph\]](#).
5. A. Ghosh, P. Konar, T. Samui, and R. K. Singh, “Jet substructure probe on scalar leptoquark models via top polarization,” *JHEP* **07** (2025) 145, [arXiv:2505.16328 \[hep-ph\]](#).
6. S. Chakraborty, M. Mitra, and S. Shil, “Fat Jet Signature of a Heavy Neutrino at Lepton Collider,” *Phys. Rev. D* **100** no. 1, (2019) 015012, [arXiv:1810.08970 \[hep-ph\]](#).
7. R. Padhan, M. Mitra, S. Kulkarni, and F. F. Deppisch, “Displaced fat-jets and tracks to probe boosted right-handed neutrinos in the $U(1)_{B-L}$ model,” *Eur. Phys. J. C* **82** no. 10, (2022) 858, [arXiv:2203.06114 \[hep-ph\]](#).
8. R. Baruah, A. Choudhury, K. Ghosh, S. Mondal, and R. Sahu, “Probing sub-TeV Higgsinos aided by a machine-learning-based top tagger in the context of trilinear R-parity violating SUSY,” *Phys. Rev. D* **111** no. 9, (2025) 095004, [arXiv:2412.11862 \[hep-ph\]](#).
9. R. Sahu, D. Sahoo, and K. Ghosh, “Advancing Higgsino Searches by Integrating ML for Boosted Object Tagging and Event Selection,” [arXiv:2501.07491 \[hep-ph\]](#).
10. G. Hiller, T. Höhne, D. F. Litim, and T. Stuedtner, “Vacuum stability in the Standard Model and beyond,” *Phys. Rev. D* **110** no. 11, (2024) 115017, [arXiv:2401.08811 \[hep-ph\]](#).

11. G. Degrassi, S. Di Vita, J. Elias-Miro, J. R. Espinosa, G. F. Giudice, G. Isidori, and A. Strumia, “Higgs mass and vacuum stability in the Standard Model at NNLO,” *JHEP* **08** (2012) 098, [arXiv:1205.6497 \[hep-ph\]](#).
12. D. Buttazzo, G. Degrassi, P. P. Giardino, G. F. Giudice, F. Sala, A. Salvio, and A. Strumia, “Investigating the near-criticality of the Higgs boson,” *JHEP* **12** (2013) 089, [arXiv:1307.3536 \[hep-ph\]](#).
13. S. Alekhin, A. Djouadi, and S. Moch, “The top quark and Higgs boson masses and the stability of the electroweak vacuum,” *Phys. Lett. B* **716** (2012) 214–219, [arXiv:1207.0980 \[hep-ph\]](#).
14. J. Elias-Miro, J. R. Espinosa, G. F. Giudice, G. Isidori, A. Riotto, and A. Strumia, “Higgs mass implications on the stability of the electroweak vacuum,” *Phys. Lett. B* **709** (2012) 222–228, [arXiv:1112.3022 \[hep-ph\]](#).
15. J. R. Espinosa, “Implications of the top (and Higgs) mass for vacuum stability,” *PoS TOP2015* (2016) 043, [arXiv:1512.01222 \[hep-ph\]](#).
16. R. Sahu, S. Ashanujjaman, and K. Ghosh, “Unveiling the secrets of new physics through top quark tagging,” *Eur. Phys. J. ST* **233** no. 15-16, (2024) 2465–2495, [arXiv:2409.12085 \[hep-ph\]](#).
17. B. Bhattacharjee, C. Bose, A. Chakraborty, and R. Sengupta, “Boosted top tagging and its interpretation using Shapley values,” *Eur. Phys. J. Plus* **139** no. 12, (2024) 1131, [arXiv:2212.11606 \[hep-ph\]](#).
18. V. Mikuni and B. Nachman, “Method to simultaneously facilitate all jet physics tasks,” *Phys. Rev. D* **111** no. 5, (2025) 054015, [arXiv:2502.14652 \[hep-ph\]](#).
19. J. Thaler and K. Van Tilburg, “Identifying Boosted Objects with N-subjettiness,” *JHEP* **03** (2011) 015, [arXiv:1011.2268 \[hep-ph\]](#).
20. J. Thaler and K. Van Tilburg, “Maximizing Boosted Top Identification by Minimizing N-subjettiness,” *JHEP* **02** (2012) 093, [arXiv:1108.2701 \[hep-ph\]](#).
21. I. W. Stewart, F. J. Tackmann, and W. J. Waalewijn, “N-Jettiness: An Inclusive Event Shape to Veto Jets,” *Phys. Rev. Lett.* **105** (2010) 092002, [arXiv:1004.2489 \[hep-ph\]](#).
22. A. J. Larkoski, G. P. Salam, and J. Thaler, “Energy Correlation Functions for Jet Substructure,” *JHEP* **06** (2013) 108, [arXiv:1305.0007 \[hep-ph\]](#).
23. I. Mould, L. Necib, and J. Thaler, “New Angles on Energy Correlation Functions,” *JHEP* **12** (2016) 153, [arXiv:1609.07483 \[hep-ph\]](#).
24. P. T. Komiske, E. M. Metodiev, and J. Thaler, “Energy flow polynomials: A complete linear basis for jet substructure,” *JHEP* **04** (2018) 013, [arXiv:1712.07124 \[hep-ph\]](#).
25. A. Abdesselam *et al.*, “Boosted Objects: A Probe of Beyond the Standard Model Physics,” *Eur. Phys. J. C* **71** (2011) 1661, [arXiv:1012.5412 \[hep-ph\]](#).
26. R. Kogler *et al.*, “Jet Substructure at the Large Hadron Collider: Experimental Review,” *Rev. Mod. Phys.* **91** no. 4, (2019) 045003, [arXiv:1803.06991 \[hep-ex\]](#).
27. A. Altheimer *et al.*, “Jet Substructure at the Tevatron and LHC: New Results, New Tools, New Benchmarks,” *J. Phys. G* **39** (2012) 063001, [arXiv:1201.0008 \[hep-ph\]](#).
28. A. Altheimer *et al.*, “Boosted Objects and Jet Substructure at the LHC. Report of BOOST2012, held at IFIC Valencia, 23rd-27th of July 2012,” *Eur. Phys. J. C* **74** no. 3, (2014) 2792, [arXiv:1311.2708 \[hep-ex\]](#).
29. D. Adams *et al.*, “Towards an Understanding of the Correlations in Jet Substructure,” *Eur. Phys. J. C* **75** no. 9, (2015) 409, [arXiv:1504.00679 \[hep-ph\]](#).
30. S. Marzani, G. Soyez, and M. Spannowsky, *Looking inside jets: an introduction to jet substructure and boosted-object phenomenology*, vol. 958. Springer, 2019. [arXiv:1901.10342 \[hep-ph\]](#).
31. A. J. Larkoski, I. Mould, and B. Nachman, “Jet Substructure at the Large Hadron Collider: A Review of Recent Advances in Theory and Machine Learning,” *Phys. Rept.* **841** (2020) 1–63, [arXiv:1709.04464 \[hep-ph\]](#).
32. P. Baldi, K. Bauer, C. Eng, P. Sadowski, and D. Whiteson, “Jet Substructure Classification in High-Energy Physics with Deep Neural Networks,” *Phys. Rev. D* **93** no. 9, (2016) 094034, [arXiv:1603.09349 \[hep-ex\]](#).
33. M. Kagan, “Image-Based Jet Analysis,” [arXiv:2012.09719 \[physics.data-an\]](#).
34. G. Kasieczka, T. Plehn, M. Russell, and T. Schell, “Deep-learning Top Taggers or The End of QCD?,” *JHEP* **05** (2017) 006, [arXiv:1701.08784 \[hep-ph\]](#).
35. S. Macaluso and D. Shih, “Pulling Out All the Tops with Computer Vision and Deep Learning,” *JHEP* **10** (2018) 121, [arXiv:1803.00107 \[hep-ph\]](#).
36. A. Butter *et al.*, “The Machine Learning landscape of top taggers,” *SciPost Phys.* **7** (2019) 014, [arXiv:1902.09914 \[hep-ph\]](#).
37. S. Diefenbacher, H. Frost, G. Kasieczka, T. Plehn, and J. M. Thompson, “CapsNets Continuing the Convolutional Quest,” *SciPost Phys.* **8** (2020) 023, [arXiv:1906.11265 \[hep-ph\]](#).
38. S. Bollweg, M. Haußmann, G. Kasieczka, M. Luchmann, T. Plehn, and J. Thompson, “Deep-Learning Jets with Uncertainties and More,” *SciPost Phys.* **8** no. 1, (2020) 006, [arXiv:1904.10004 \[hep-ph\]](#).

39. A. Butter, G. Kasieczka, T. Plehn, and M. Russell, “Deep-learned Top Tagging with a Lorentz Layer,” *SciPost Phys.* **5** no. 3, (2018) 028, [arXiv:1707.08966 \[hep-ph\]](#).
40. J. Shlomi, P. Battaglia, and J.-R. Vlimant, “Graph Neural Networks in Particle Physics,” [arXiv:2007.13681 \[hep-ex\]](#).
41. J. Duarte and J.-R. Vlimant, “Graph Neural Networks for Particle Tracking and Reconstruction,” [arXiv:2012.01249 \[hep-ph\]](#).
42. S. Thais, P. Calafiura, G. Chachamis, G. DeZoort, J. Duarte, S. Ganguly, M. Kagan, D. Murnane, M. S. Neubauer, and K. Terao, “Graph Neural Networks in Particle Physics: Implementations, Innovations, and Challenges,” in *Snowmass 2021*. 3, 2022. [arXiv:2203.12852 \[hep-ex\]](#).
43. P. T. Komiske, E. M. Metodiev, and J. Thaler, “Energy Flow Networks: Deep Sets for Particle Jets,” *JHEP* **01** (2019) 121, [arXiv:1810.05165 \[hep-ph\]](#).
44. H. Qu and L. Gouskos, “ParticleNet: Jet Tagging via Particle Clouds,” *Phys. Rev. D* **101** no. 5, (2020) 056019, [arXiv:1902.08570 \[hep-ph\]](#).
45. A. Bogatskiy, B. Anderson, J. T. Offermann, M. Roussi, D. W. Miller, and R. Kondor, “Lorentz Group Equivariant Neural Network for Particle Physics,” [arXiv:2006.04780 \[hep-ph\]](#).
46. S. Gong, Q. Meng, J. Zhang, H. Qu, C. Li, S. Qian, W. Du, Z.-M. Ma, and T.-Y. Liu, “An efficient Lorentz equivariant graph neural network for jet tagging,” *JHEP* **07** (2022) 030, [arXiv:2201.08187 \[hep-ph\]](#).
47. A. Bogatskiy, T. Hoffman, D. W. Miller, J. T. Offermann, and X. Liu, “Explainable equivariant neural networks for particle physics: PELICAN,” *JHEP* **03** (2024) 113, [arXiv:2307.16506 \[hep-ph\]](#).
48. A. Bogatskiy, T. Hoffman, D. W. Miller, and J. T. Offermann, “PELICAN: Permutation Equivariant and Lorentz Invariant or Covariant Aggregator Network for Particle Physics,” [arXiv:2211.00454 \[hep-ph\]](#).
49. A. Bogatskiy, T. Hoffman, and J. T. Offermann, “19 Parameters Is All You Need: Tiny Neural Networks for Particle Physics,” in *37th Conference on Neural Information Processing Systems*. 10, 2023. [arXiv:2310.16121 \[hep-ph\]](#).
50. A. Vaswani, N. Shazeer, N. Parmar, J. Uszkoreit, L. Jones, A. N. Gomez, L. Kaiser, and I. Polosukhin, “Attention is all you need,” *CoRR* **abs/1706.03762** (2017), [1706.03762](#). <http://arxiv.org/abs/1706.03762>.
51. C. K. Joshi, “Transformers are Graph Neural Networks,” *arXiv e-prints* (June, 2025) [arXiv:2506.22084](#), [arXiv:2506.22084 \[stat.ML\]](#).
52. H. Qu, C. Li, and S. Qian, “Particle Transformer for Jet Tagging,” [arXiv:2202.03772 \[hep-ph\]](#).
53. V. Mikuni and F. Canelli, “Point cloud transformers applied to collider physics,” *Mach. Learn. Sci. Tech.* **2** no. 3, (2021) 035027, [arXiv:2102.05073 \[physics.data-an\]](#).
54. Y. Wu, K. Wang, C. Li, H. Qu, and J. Zhu, “Jet tagging with more-interaction particle transformer*,” *Chin. Phys. C* **49** no. 1, (2025) 013110, [arXiv:2407.08682 \[hep-ph\]](#).
55. V. Mikuni and B. Nachman, “Solving key challenges in collider physics with foundation models,” *Phys. Rev. D* **111** no. 5, (2025) L051504, [arXiv:2404.16091 \[hep-ph\]](#).
56. W. Bhimji, C. Harris, V. Mikuni, and B. Nachman, “OmniLearned: A Foundation Model Framework for All Tasks Involving Jet Physics,” [arXiv:2510.24066 \[hep-ph\]](#).
57. J. Spinner, V. Bresó, P. de Haan, T. Plehn, J. Thaler, and J. Brehmer, “Lorentz-Equivariant Geometric Algebra Transformers for High-Energy Physics,” in *38th conference on Neural Information Processing Systems*. 10, 2024. [arXiv:2405.14806 \[physics.data-an\]](#).
58. J. Brehmer, V. Bresó, P. de Haan, T. Plehn, H. Qu, J. Spinner, and J. Thaler, “A Lorentz-equivariant transformer for all of the LHC,” *SciPost Phys.* **19** no. 4, (2025) 108, [arXiv:2411.00446 \[hep-ph\]](#).
59. Y. Lecun, L. Bottou, Y. Bengio, and P. Haffner, “Gradient-based learning applied to document recognition,” *Proceedings of the IEEE* **86** no. 11, (1998) 2278–2324.
60. K. He, X. Zhang, S. Ren, and J. Sun, “Deep residual learning for image recognition,” in *2016 IEEE Conference on Computer Vision and Pattern Recognition (CVPR)*, pp. 770–778. 2016.
61. M. Tan and Q. Le, “Efficientnet: Rethinking model scaling for convolutional neural networks,” in *International conference on machine learning*, pp. 6105–6114, PMLR. 2019.
62. M. Tan and Q. Le, “Efficientnetv2: Smaller models and faster training,” in *International conference on machine learning*, pp. 10096–10106, PMLR. 2021.
63. A. G. Howard, M. Zhu, B. Chen, D. Kalenichenko, W. Wang, T. Weyand, M. Andreetto, and H. Adam, “Mobilenets: Efficient convolutional neural networks for mobile vision applications,” *arXiv preprint arXiv:1704.04861* (2017).
64. M. Sandler, A. Howard, M. Zhu, A. Zhmoginov, and L.-C. Chen, “Mobilenetv2: Inverted residuals and linear bottlenecks,” in *Proceedings of the IEEE conference on computer vision and pattern recognition*, pp. 4510–4520. 2018.
65. A. Howard, M. Sandler, *et al.*, “Searching for mobilenetv3,” in *Proceedings of the IEEE/CVF*

- international conference on computer vision*, pp. 1314–1324. 2019.
66. D. Qin, C. Leichner, *et al.*, “Mobilenetv4: Universal models for the mobile ecosystem,” in *European Conference on Computer Vision*, pp. 78–96, Springer. 2024.
 67. M. Tan, B. Chen, R. Pang, V. Vasudevan, M. Sandler, A. Howard, and Q. V. Le, “Mnasnet: Platform-aware neural architecture search for mobile,” in *Proceedings of the IEEE/CVF conference on computer vision and pattern recognition*, pp. 2820–2828. 2019.
 68. T. Smith and J. Guild, “The C.I.E. colorimetric standards and their use,” *Transactions of the Optical Society* **33** no. 3, (Jan., 1931) 73–134.
 69. Q. L. M. Tan, “EfficientNet Trained on ImageNet.” 2020. <https://resources.wolframcloud.com/NeuralNetRepository/resources/EfficientNet-Trained-on-ImageNet/>. [Accessed: 30-September-2025].
 70. T. Sjöstrand, S. Ask, J. R. Christiansen, R. Corke, N. Desai, P. Ilten, S. Mrenna, S. Prestel, C. O. Rasmussen, and P. Z. Skands, “An introduction to PYTHIA 8.2” *Comput. Phys. Commun.* **191** (2015) 159–177, [arXiv:1410.3012](https://arxiv.org/abs/1410.3012) [hep-ph].
 71. DELPHES 3 Collaboration, J. de Favereau, C. Delaere, P. Demin, A. Giammanco, V. Lemaître, A. Mertens, and M. Selvaggi, “DELPHES 3, A modular framework for fast simulation of a generic collider experiment,” *JHEP* **02** (2014) 057, [arXiv:1307.6346](https://arxiv.org/abs/1307.6346) [hep-ex].
 72. M. Cacciari, G. P. Salam, and G. Soyez, “The anti- k_t jet clustering algorithm,” *JHEP* **04** (2008) 063, [arXiv:0802.1189](https://arxiv.org/abs/0802.1189) [hep-ph].
 73. M. Cacciari, G. P. Salam, and G. Soyez, “FastJet User Manual,” *Eur. Phys. J. C* **72** (2012) 1896, [arXiv:1111.6097](https://arxiv.org/abs/1111.6097) [hep-ph].
 74. ATLAS Collaboration, “Identification of hadronically-decaying top quarks using UFO jets with ATLAS in Run 2,” tech. rep., CERN, Geneva, 2021. <https://cds.cern.ch/record/2776782>. All figures including auxiliary figures are available at <https://atlas.web.cern.ch/Atlas/GROUPS/PHYSICS/PUBNOTES/ATL-PHYS-PUB-2021-028>.
 75. A. J. Larkoski, I. Moult, and D. Neill, “Power Counting to Better Jet Observables,” *JHEP* **12** (2014) 009, [arXiv:1409.6298](https://arxiv.org/abs/1409.6298) [hep-ph].
 76. A. J. Larkoski, I. Moult, and D. Neill, “Analytic Boosted Boson Discrimination,” *JHEP* **05** (2016) 117, [arXiv:1507.03018](https://arxiv.org/abs/1507.03018) [hep-ph].
 77. A. J. Larkoski, I. Moult, and D. Neill, “Building a Better Boosted Top Tagger,” *Phys. Rev. D* **91** no. 3, (2015) 034035, [arXiv:1411.0665](https://arxiv.org/abs/1411.0665) [hep-ph].
 78. A. Krizhevsky, I. Sutskever, and G. E. Hinton, “Imagenet classification with deep convolutional neural networks,” in *Advances in Neural Information Processing Systems*, F. Pereira, C. Burges, L. Bottou, and K. Weinberger, eds., vol. 25. Curran Associates, Inc., 2012. https://proceedings.neurips.cc/paper_files/paper/2012/file/c399862d3b9d6b76c8436e924a68c45b-Paper.pdf.
 79. C. Szegedy, W. Liu, Y. Jia, P. Sermanet, S. Reed, D. Anguelov, D. Erhan, V. Vanhoucke, and A. Rabinovich, “Going deeper with convolutions,” in *2015 IEEE Conference on Computer Vision and Pattern Recognition (CVPR)*, pp. 1–9. 2015.
 80. C. Szegedy, V. Vanhoucke, S. Ioffe, J. Shlens, and Z. Wojna, “Rethinking the inception architecture for computer vision,” in *2016 IEEE Conference on Computer Vision and Pattern Recognition (CVPR)*, pp. 2818–2826. 2016.
 81. S. Zagoruyko and N. Komodakis, “Wide residual networks,” *arXiv preprint arXiv:1605.07146* (2016).
 82. G. Huang, Z. Liu, L. Van Der Maaten, and K. Q. Weinberger, “Densely connected convolutional networks,” in *2017 IEEE Conference on Computer Vision and Pattern Recognition (CVPR)*, pp. 2261–2269. 2017.
 83. C. Szegedy, S. Ioffe, V. Vanhoucke, and A. Alemi, “Inception-v4, inception-resnet and the impact of residual connections on learning,” *Proceedings of the AAAI Conference on Artificial Intelligence* **31** no. 1, (Feb., 2017). <https://ojs.aaai.org/index.php/AAAI/article/view/11231>.
 84. S. Xie, R. Girshick, P. Dollár, Z. Tu, and K. He, “Aggregated residual transformations for deep neural networks,” in *2017 IEEE Conference on Computer Vision and Pattern Recognition (CVPR)*, pp. 5987–5995. 2017.
 85. K. Yang, K. Qinami, L. Fei-Fei, J. Deng, and O. Russakovsky, “Towards fairer datasets: Filtering and balancing the distribution of the people subtree in the imagenet hierarchy,” in *Conference on Fairness, Accountability, and Transparency*. 2020.
 86. K. Yang, J. Yau, L. Fei-Fei, J. Deng, and O. Russakovsky, “A study of face obfuscation in imagenet,” in *International Conference on Machine Learning (ICML)*. 2022.
 87. J. Long, E. Shelhamer, and T. Darrell, “Fully convolutional networks for semantic segmentation,” in *Proceedings of the IEEE conference on computer vision and pattern recognition*, pp. 3431–3440. 2015.
 88. J. Hu, L. Shen, and G. Sun, “Squeeze-and-excitation networks,” in *Proceedings of the IEEE conference on computer vision and pattern recognition*,

pp. 7132–7141. 2018.

89. D. P. Kingma, “Adam: A method for stochastic optimization,” *arXiv preprint arXiv:1412.6980* (2014) .